Kobe University Repository : Kernel

PDF issue: 2026-11-25

Solvent reverse osmosis beyond size exclusion in two-dimensional nanochannel membranes

Guan, Kecheng ; Guo, Yuanyuan ; Dai, Liheng ; Zhang, Aiwen ; Li, Zhan ; Deng, Erda ; Nakagawa, Keizo ; Guo, Yanan ; Liu, Gongping ; Yoshioka,…

(Citation)
Nature Communications,17(1):6657

(Issue Date)
2026-05-20

(Resource Type)
journal article

(Version)
Version of Record

(Rights)
© The Author(s) 2026.
This article is licensed under a Creative Commons Attribution-NonCommercial-NoDerivatives 4.0 International License, which permits any non-commercial use, sharing, distribution and reproduction in any medium or format, as long as you give…

(URL)
https://hdl.handle.net/20.500.14094/0100505096

nature communications

Article

https://doi.org/10.1038/s41467-026-73466-6

Solvent reverse osmosis beyond size exclusion in two-dimensional nanochannel membranes

Received: 30 October 2025

Accepted: 8 May 2026

Published online: 20 May 2026

Check for updates

Kecheng Guan[1], Yuanyuan Guo[2], Liheng Dai[1], Aiwen Zhang[1,3], Zhan Li[1], Erda Deng[1], Keizo Nakagawa[1,4], Yanan Guo[2] ✉, Gongping Liu[2], Tomohisa Yoshioka[1,4], Wanqin Jin[2] ✉ & Hideto Matsuyama[1,3] ✉

Solvent reverse osmosis is a pressure-driven, liquid-phase process for separating solvent mixtures, offering a potential low-energy alternative to thermal operations. Graphene oxide (GO) laminates provide tunable nanochannels to probe confined solvent transport, yet solvent–solvent separations remain underexplored due to solvation-induced structural instabilities and the small molecular sizes. Here we construct solvent-stable, supported GO nanochannel membranes that preserves integrity under pressurized solvents, and tune interlayer confinement and surface polarity via controlled chemical reduction. Across 51 solvent systems and 5 distinct nanochannels, we demonstrate that separation is governed by coupled nanoconfinement and solvent affinity, where selective interfacial association can surpass simple size-exclusion expectations. Maximum permselectivity arises from balancing channel size with retained polarity, indicating that channel shrinking alone does not optimize performance. These findings identify channel surface chemistry as a key design factor for polarity-rich solvent systems and provide a framework for rationally tailoring nanochannels for complex solvent separations.

Separating solvent mixtures is among the most energy-intensive operations in the chemical industry[1], as conventional distillation relies on phase-change processes that require substantial energy input. Solvent reverse osmosis[2], while explored in earlier studies[3,4], has only recently attracted renewed attention[5–11] for its potential to provide energy-efficient liquid-phase separations with significantly lower energy demands. This renewed interest has been driven by advances in membrane materials and the urgent need for low-carbon alternatives to distillation in response to rising energy and sustainability concerns[12–14]. Reverse osmosis already accounts for around 70% of the global desalination market because of its pronounced energy efficiency[15], and similar benefits may be expected for solvent separation[9]. Nevertheless, solvent reverse osmosis remains underdeveloped compared with aqueous desalination, with existing research limited to a narrow range of membrane types and systematic analyses of transport and selectivity largely absent.

The promise of solvent reverse osmosis relies on nanoscale transport phenomena. At the nanoscale, confinement and interfacial effects alter molecular behavior[16–18] across diverse systems. In membranes, such spatial restrictions reshape local solvent organization and accessible transport pathways beyond simple size exclusion. Inspired by biological ion channels and synthetic nanopores[19,20], synthetic membranes with tailored nanochannels[21,22] can leverage geometric confinement and pore-wall chemistry to separate species with subtle differences. Layered two-dimensional (2D) materials[23] with tunable interlayer spacing provide particularly versatile platforms, as their

[1]Research Center for Membrane and Film Technology, Kobe University, Kobe, Japan. [2]State Key Laboratory of Materials-Oriented Chemical Engineering, College of Chemical Engineering, Nanjing Tech University, Nanjing, China. [3]Department of Chemical Science and Engineering, Kobe University, Kobe, Japan. [4]Graduate School of Science, Technology and Innovation, Kobe University, Kobe, Japan. ✉e-mail: guoyn@njtech.edu.cn; wqjin@njtech.edu.cn; matuyama@kobe-u.ac.jp

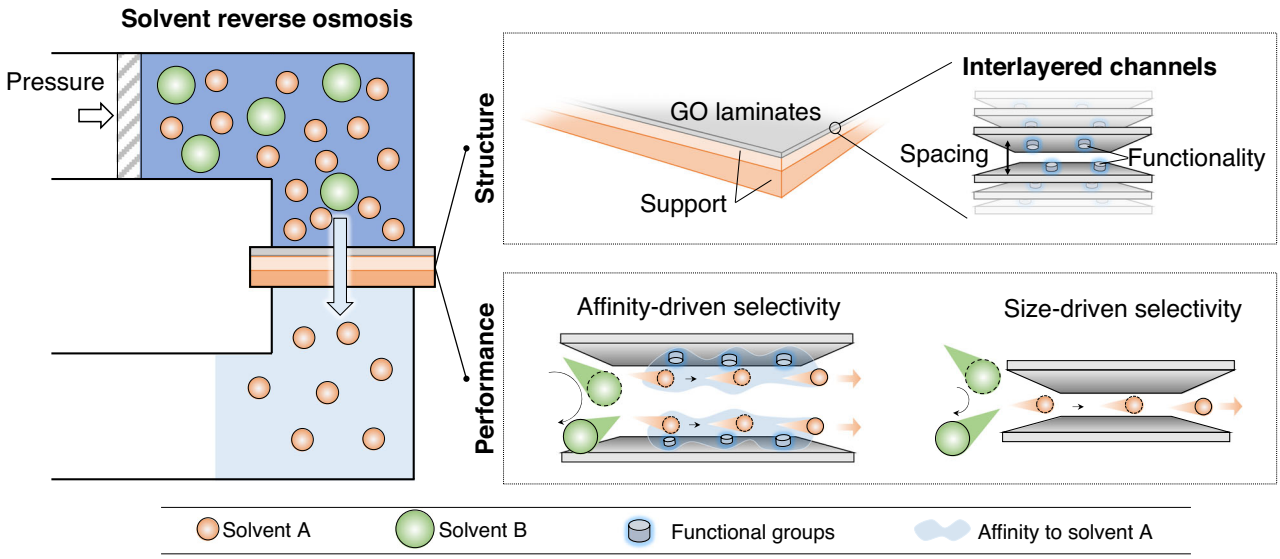

Fig. 1 | Solvent reverse osmosis through supported GO nanochannels. Schematic of solvent reverse osmosis, supported GO nanochannel membranes, and solvent transport driven by affinity and size.

laminar channels combine structural definition with adjustable surface functionality. In aqueous and ionic systems, such channels achieve remarkable separation performance[24–27] through size exclusion, dielectric exclusion, and electrostatic interactions, enabling even monovalent ions of nearly identical size and charge to be distinguished[28–30]. Insights from these systems suggest that precise separation need not rely solely on size exclusion, raising the prospect that similar confined-transport mechanisms could be applied to solvent reverse osmosis.

Solvent transport in nanochannels presents an equally intriguing but distinct challenge. Intermolecular and interfacial interactions, along with the orientational ordering of confined solvent molecules significantly influence solvent flow behavior[31,32]. Deviations from classical viscosity further contribute to nonlinear transport that cannot be captured by continuum models such as the Hagen–Poiseuille equation[33,34]. As a result, separation in such confined spaces therefore arises not only from size exclusion but also from differences in solvent–channel affinity, affecting local composition and molecular organization within nanochannels and altering transport barriers. Unlike aqueous systems, solvent mixtures involve more diverse molecular combinations and interaction patterns, and the chemical harshness of organic solvents further challenges nanochannel stability. Consequently, solvent–solvent separations in 2D membranes remain largely unexplored. Most prior solvent transport-related studies have primarily focused on organic solvent nanofiltration[35,36] for removing solutes such as dyes and pharmaceuticals, where separation is largely enabled by size differences between solutes and solvents[37]. By contrast, solvent–solvent systems involve comparable molecular sizes, necessitating selectivity through confined affinity effects within well-defined nanochannels.

Recent affinity-engineered cross-linked polymer membranes demonstrate that tailoring pore–solvent interactions can enhance selectivity beyond size exclusion in solvent–solvent separations[38,39]. However, extracting general design rules from such systems is often nontrivial, because changes in pore chemistry introduced through monomer substitution may co-vary with structurally heterogeneous pore network and solvent-induced structural responses, obscuring interpretation across chemically diverse solvents. Layered 2D membranes provide a desirable platform, in which a common laminated transport geometry enables confinement and interfacial chemistry to be tuned in a structurally consistent manner. This structural definition facilitates systematic analysis of structure–transport relationships. Importantly, viewing these confined channels as a well-defined building block yields principles that can be translated to other confined pore architectures, informing how affinity and confinement should be co-engineered for solvent reverse osmosis.

In this study, we report a robust thin-film composite design of polymer-supported graphene oxide (GO) nanochannel membranes, engineered to maintain structural integrity under high-pressure solvent conditions for reverse osmosis separation of solvent mixtures (Fig. 1). The design decouples macro- and microstructural engineering by pairing a solvent-resistant support that suppresses solvent-dependent deformation, while controlled chemical reduction regulates GO nanochannel functionality. This platform enables systematic investigation of solvent mixture separations under nanoconfinement, allowing cross-examinations between tunable nanochannel states and chemically diverse solvent families under solvent reverse osmosis conditions. By testing a broad spectrum of polar and nonpolar solvent combinations, we demonstrate that efficient separation of molecularly similar solvent mixtures can be achieved through finely tuned GO nanochannels. The results reveal that separation is governed by both size exclusion and solvent–channel interactions set by channel-wall chemistry and solvent polarity. We identify the conditions where retained channel affinity and controlled confinement work together to maximize permselectivity, clarifying when laminated 2D membranes can deliver robust solvent reverse osmosis performance and when additional structural reinforcement is required.

Results

Macrostructural configuration of supported GO membranes

Thin free-standing GO laminates are too fragile for practical filtrations due to their poor mechanical strength. For high-pressure processes like reverse osmosis, GO is therefore integrated with porous supports. Compared to reverse osmosis desalination, solvent separation imposes stricter requirements on supports due to wide variety of solvents and higher operating pressures involved. Different solvents can induce varying degrees of swelling in the support, leading to macrostructural deformations when the feed solvent changes. Under high pressure, these deformations may become mechanically compressed, potentially causing irreversible damage to the support, which in turn destabilize the supported GO layer.

To investigate the role of porous supports, we compared two different solvent-resistant polymer membranes (Supplementary Fig. 1): commercially available nylon and homemade aliphatic polyketone (PK)[9,40]. While nylon is widely used, its mechanical properties varied strongly with solvent type, showing large differences after wetting with water, methanol, or hexane (Fig. 2a). This indicates that its structural integrity varies depending on the solvent environment, leading to inconsistent support properties. PK (Supplementary Fig. 1), by contrast, maintained relatively consistent mechanical properties across solvents (Fig. 2a). Identical GO laminates (GO here was treated by 20 min chemical reduction; see details in Methods) were deposited on nylon and PK to form thin-film composite membrane structures of GO/nylon and GO/PK, respectively. Under water and methanol filtration at 30 bar using a crossflow filtration setup (Supplementary Fig. 2), both membranes compacted, but GO/nylon showed stronger permeance decline, unstable responses to solvent exchange, and frequent wrinkling, whereas GO/PK was more stable (Fig. 2b, c). To further suppress deformation, PK was reinforced with polyester fabric (PK/fabric), yielding GO/PK/fabric membranes with minimal compaction and stable permeance during solvent changes (Fig. 2d).

These results demonstrate that solvent-induced swelling of the support directly governs the macrostructural stability of the GO layer. Inconsistent support deformations create elastic stress that cannot be released in sealed cells, resulting in wrinkling[41] and eventual defects (Fig. 2e). A preliminary separation test with a 95 wt% methanol and 5 wt % methyl tert-butyl ether (MTBE) at 30 bar confirmed this (Supplementary Fig. 3): GO/nylon failed, while GO/PK and GO/PK/fabric achieved ~77% and ~87% MTBE rejection, respectively. Given its robust stability and performance, PK/fabric-supported GO membrane was selected for subsequent studies.

Using PK/fabric as the support, we evaluated the morphology of the supported GO membrane. Scanning electron microscope (SEM) analysis revealed that GO layer exhibited a thickness of less than 100 nm (appearing as light purple in the false-color SEM images, Fig. 2f) with a deposition density of ~0.12 g m^{-2}. After immersion for 24 days in solvents including methanol, dimethylformamide (DMF), n-hexane, and toluene, the GO layer remained intact with no detachment or visible damage (Fig. 2f and Supplementary Figs. 4, 5), confirming sufficient solvent resistance for solvent separation applications.

Microstructure and chemistry control of GO layer

The supported laminated GO architecture enables high-pressure solvent permeation testing across solvents by decoupling support swelling from interlayer nanochannel evolution, a prerequisite for establishing reliable structure–transport correlations in 2D laminates. In 2D membranes, nanochannels are formed by nanosheet stacking, making nanosheet chemistry[42] a key factor in determining channel size and surface properties. Understanding how solvent transport behavior changes in controlled nanochannels provides valuable insights into solvent mixture separation by 2D membranes. To tailor these properties, GO was reduced using glucose in aqueous ammonia for different durations (0, 10, 20, 30, and 60 min), yielding T0 (namely original GO), T10, T20, T30, and T60 membranes.

The controlled removal of oxygenated functional groups from GO was evidenced by a decline in the O/C ratio measured by X-ray photoelectron spectroscopy (XPS, Fig. 3a and Supplementary Fig. 6). A slightly higher O/C ratio was observed for T10 compared to pristine GO (T0), which is attributed to the very low reduction degree at the early stage and the presence of residual glucose-derived species. Because glucose (O/C = 1) was used as the reducing agent, trace amounts of adsorbed or partially reacted glucose can contribute to the XPS signal when the extent of GO reduction is still limited.

This chemical change was accompanied by structural densification, as X-ray diffraction (XRD, Fig. 3b and Supplementary Fig. 7)

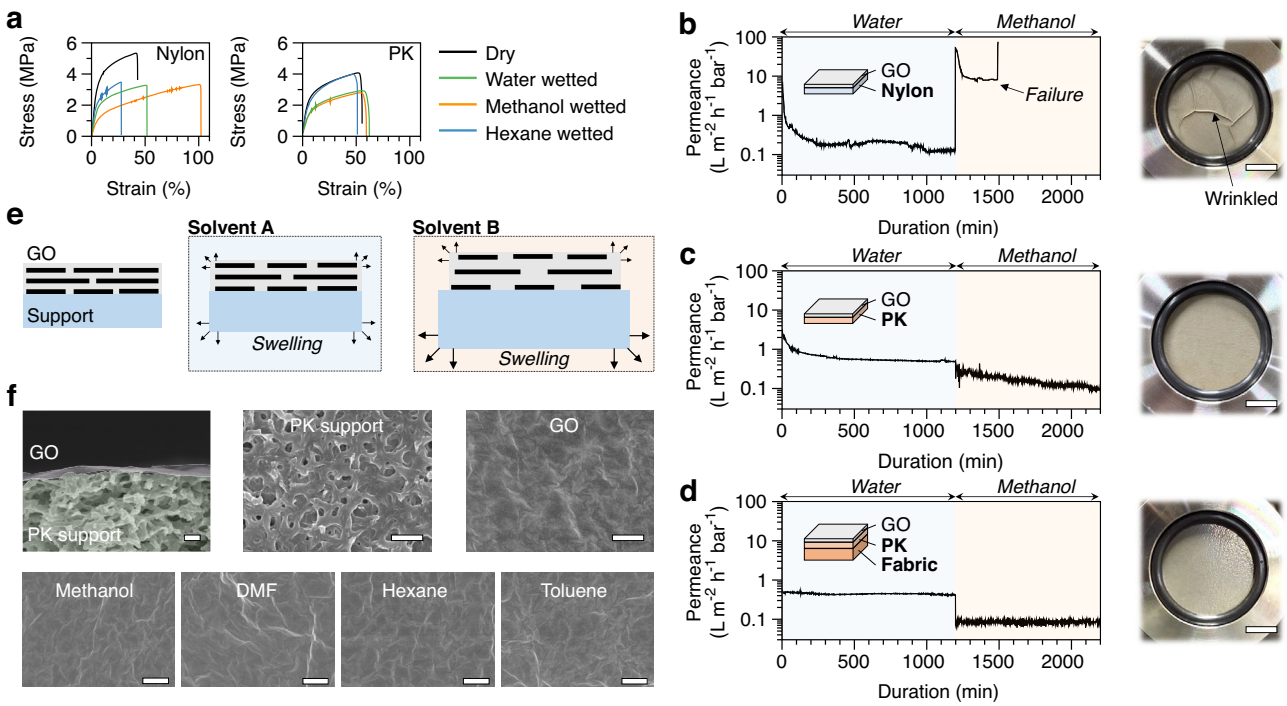

Fig. 2 | Thin-film composite architecture and solvent-induced responses of supported GO membranes. a Stress-strain curves of porous nylon and PK supports before and after solvent wetting. Time-dependent permeance during sequential water and methanol permeation for GO membranes supported on (**b**) nylon, (**c**) PK, and (**d**) PK/fabric, along with digital photos of sealed membrane coupons after permeation tests (scale bars: 1 cm). GO membranes reduced for 20 min were used for all composite membranes in (**b**–**d**). **e** Schematic illustrating deformation modes of the thin-film composite structure under different conditions. **f** Cross-sectional SEM image of a supported GO membrane and surface SEM images of the PK support and GO selective layer before and after solvent immersion (scale bars: 1 μm).

https://doi.org/10.1038/s41467-026-73466-6

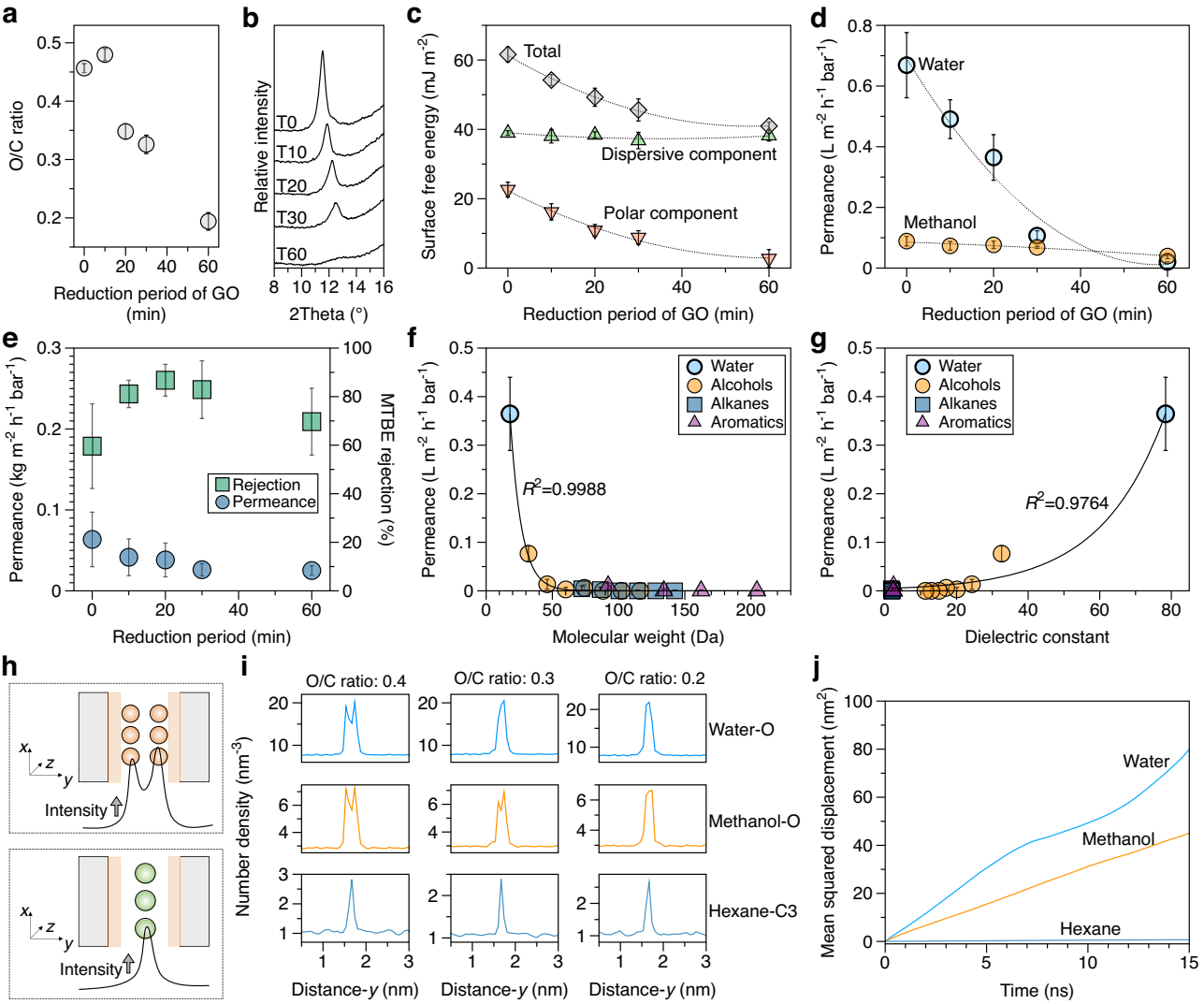

Fig. 3 | GO nanochannel properties and solvent transport under confinement. **a** O/C ratio, (**b**) XRD patterns, (**c**) surface free energy, (**d**) water and methanol permeance, and (**e**) MTBE/methanol separation performance of GO membranes prepared with different chemical reduction periods. Dotted lines in (**c**, **d**) serve as visual guides. **f**, **g** Dependence of solvent permeance of the T20 membrane on (**f**) molecular weight and (**g**) dielectric constant. Data were fitted using an exponential growth function; corresponding R^2 values are shown in the figure. Error bars represent the mean ± standard deviation ($n = 2$–4 independent replicates per condition). **h** Schematic of two representative solvent distributions within GO nanochannels along the membrane thickness direction. **i** Number density profiles along the membrane thickness direction for water oxygen (Water-O), methanol oxygen (Methanol-O), and the third carbon atom of hexane (Hexane-C3) in GO nanochannels at three oxidation degrees (GO40, GO30, GO20); number density profiles of all hexane carbon atoms are shown in Supplementary Fig. 23. **j** Mean square displacement of water, methanol, and hexane in GO40 nanochannels. Note: All permeation and separation tests were performed at 30 bar. Pure-solvent permeance is reported on a volumetric basis (L m^{-2} h^{-1} bar^{-1}), whereas mixture permeance is reported on a mass basis (kg m^{-2} h^{-1} bar^{-1}).

revealed systematic peak shifts toward smaller *d*-spacing (Supplementary Table 1). The effective free space within the 2D nanochannels, which governs molecular transport, was estimated by subtracting the thickness of a single graphene sheet (0.34 nm) from the measured *d*-spacing. With increasing reduction degree, this free space decreased from 0.43 nm in T0 to 0.34 nm in T60, reflecting progressive channel densification. For the T60 membrane, the diffraction peak became significantly weakened, consistent with a high degree of reduction and reduced long-range lamellar order.

Reduced GO also showed enhanced resistance to solvent-induced swelling, whereas pristine GO exhibited substantial interlayer expansion, particularly in polar solvents. The free space in the interlayers decreased from 0.93, 0.84, and 0.43 nm for T0 to minimum values of 0.34, 0.40, and 0.38 nm for reduced GO when wetted with water, methanol, and n-hexane, respectively (Supplementary Fig. 8 and Supplementary Table 1). It should be noted that these values represent average structural parameters derived from XRD measurements, rather than the instantaneous or local channel size under pressurized solvent permeation conditions. Notably, while overall swelling was suppressed upon reduction, the solvent-dependent response evolved with increasing reduction degree. In highly reduced GO (T60), interlayer expansion induced by methanol and hexane became relatively more apparent compared to water, reflecting the diminished role of polar interactions and the increased accessibility of low-polarity channels to weakly interacting solvents.

Beyond shrinking the channels physically, chemical reduction also weakened surface polarity. Surface free energy analysis (Fig. 3c and Supplementary Fig. 9) showed a marked decline in the polar component from 22.6 to 2.6 mJ m^{-2} with extended reduction period, a trend further supported by simulation results indicating decreased molecular polarizability index with a lower O/C ratio (Supplementary Figs. 10, 11). In the experimental analysis, the reduction period is

adopted as the primary variable for correlating properties of different GO samples, as it provides well-controlled and consistent basis for comparison across samples. The corresponding O/C ratios obtained from XPS serve as chemical descriptors of the reduction degree and are used to guide the construction of the molecular simulation models.

Pure solvent permeation tests highlighted the consequences of these structural and chemical changes. Water permeance dropped sharply with increasing reduction, reflecting both reduced channel size and lower polarity (Fig. 3d). Methanol showed a similar but less pronounced trend, being initially slower than water in more polar membranes (T0–T20) but comparable in less polar ones (T30, T60). Pristine GO (T0) was relatively unstable[43,44], displaying swelling-induced compaction and unusually high hexane permeance under pressure (Supplementary Figs. 12, 13). In contrast, reduced GO membranes suppressed hexane permeance to minimal levels (< 0.01 L m^{-2} h^{-1} bar^{-1}). Overall, except for T0, polar solvents consistently permeated faster in more polar membranes (T10 and T20 with polar components of surface energy of 16.2 and 10.9 mJ m^{-2}, respectively), while this polarity-driven preference weakened in the less polar T30 (8.8 mJ m^{-2}) and T60 (2.8 mJ m^{-2}) membranes.

Binary mixture tests using MTBE/methanol (5:95, w/w, minor/major) further revealed an optimal balance. Despite the relatively small difference of molecular weight and molar diameter between MTBE (88 Da, 0.72 nm, Supplementary Table 2) and methanol (32 Da, 0.51 nm, Supplementary Table 2), MTBE rejection reached a maximum of 87% in T20 (Fig. 3e), where channel size remained small enough to hinder MTBE yet polarity was still sufficient to favor methanol. In contrast, T0 and T60 showed moderate rejection (~ 60–70%), but through different mechanisms. T0 relies more on polarity contribution, whereas T60 relied on size restriction. This tradeoff underscores that effective separation requires tuning both channel confinement and wall polarity, allowing precision that surpasses conventional nanofiltration membranes, which generally target solutes larger than 1 nm[45].

To generalize these findings, permeation of 18 solvents covering water, alcohols (methanol, ethanol, propanol, butanol, pentanol, hexanol, and heptanol), alkanes (pentane, hexane, heptane, octane, nonane, and decane), and aromatics (toluene, tert-butylbenzene (TBB), 1,3-diisopropylbenzene (DIPB), and 1,3,5-triisopropylbenzene (TIPB)) (Supplementary Table 2) was measured on T20. Unless otherwise noted, all alcohols and alkanes tested were in their n-isomeric forms, and the prefix "n-" is omitted for clarity. Among the solvent descriptors analyzed, viscosity alone (Supplementary Fig. 14) showed little predictive power, diverging from continuum expectations. By contrast, molecular weight (Fig. 3f), dielectric constant (Fig. 3g), and a combined descriptor[46] (Supplementary Fig. 15) correlated strongly with permeance, although not linearly, highlighting the distinctive nature of confined transport compared with prior reports on 2D membranes[47,48] or other polymeric membranes[36,46]. Consistently, molar diameter displayed a comparable correlation trend with permeance (Supplementary Fig. 16), which is expected given its intrinsic relationship with molecular weight (see calculations in Supplementary Table 2). Here, molecular weight is therefore adopted as a solvent-independent, size-related descriptor to enable consistent comparison across chemically diverse solvent systems, in preference to gas-phase kinetic diameters or solvent-dependent hydrodynamic diameters. Similar correlations were observed for the T10 membrane (Supplementary Fig. 17). For less polar and more confined channels (T30 and T60), these trends weakened, particularly for water, again emphasizing the critical role of polarity (Supplementary Figs. 18, 19). For pristine GO (T0), no clear correlations were observed due to its large, deformable channels (Supplementary Fig. 20).

Molecular dynamics simulations[49,50] were conducted to further interpret these permeation behaviors. The overall simulation workflow is illustrated in Supplementary Fig. 21, and the constructed GO channel models with different oxidation degrees and *d*-spacings are shown in Supplementary Fig. 10. In the highly oxidized, wider channel (GO40, O/C ratio of 0.4), water and methanol preferentially accumulated at the channel walls, forming interfacial layers, while hexane localized at the center (Fig. 3h–i and Supplementary Figs. 22–23). Binding energy analysis confirmed stronger affinity of water (−12.82 kcal mol^{-1}) and methanol (−13.78 kcal mol^{-1}) with GO compared to hexane (−6.17 kcal mol^{-1}) (Supplementary Fig. 24). In less oxidized, narrower channels (GO30, O/C ratio of 0.3; GO20, O/C ratio of 0.2), this polarity-driven segregation diminished and all solvents shifted towards central monolayer-like distributions (Fig. 3i), indicating that polarity-governed spatial organization is suppressed under strong confinement. Diffusivity analysis showed that water and methanol remained more mobile than hexane even in reduced channels (Fig. 3j and Supplementary Fig. 25), suggesting that interfacial affinity facilitates rather than impedes transport for polar solvents.

Together, these results demonstrate that solvent transport in GO membranes cannot be explained by size-exclusion alone. Instead, a polarity-mediated interplay between interfacial interactions, molecular mobility, and accessible channel space governs permeation and separation, rationalizing why T20, with intermediate size and polarity, achieves optimal performance.

Solvent separation from methanol mixture in nanochannels

Since solvent transport depends on both molecular size and polarity, we first examined the separation of binary mixtures of 95 wt% methanol with 5 wt% another larger alcohol (ranging from ethanol to heptanol). Alcohol rejection increased progressively from ethanol to heptanol across all GO membranes (Fig. 4a), consistent with larger size and lower polarity of longer-chain alcohols (Supplementary Figs. 26, 27). Among the membranes, T20 again showed the highest rejection, consistent with its optimal performance in MTBE/methanol separation (Fig. 3e). Importantly, rejection improved from T0 to T20 but declined from T20 to T60, indicating that decreasing channel size alone does not guarantee improved selectivity. Instead, the balance between size and polarity is critical.

To further probe polarity effects, binary mixtures of 95 wt% methanol with alkanes (pentane, hexane, heptane, octane, nonane, or decane) or aromatics (toluene, TBB, DIPB, or TIPB) were tested across different GO membranes. Rejection increased with molecular weight (Fig. 4b and Supplementary Figs. 28–31), confirming a size contribution. Yet, when comparing alkanes (C_nH_{2n+2}) and alcohols ($C_{n-1}H_{2n}O$) of similar molecular weight (e.g., pentane *vs* butanol, hexane *vs* pentanol), the alkanes were consistently more strongly rejected (Fig. 4c–d and Supplementary Figs. 32–33). This contrast highlights polarity difference within solvent mixtures as an additional determinant. The effect was most pronounced for smaller molecules, as low-molecular-weight alcohols resemble methanol in polarity, making them harder to reject, whereas nonpolar alkanes maintain a consistently large polarity gap, enabling more effective separation.

Molecular dynamics simulations supported these observations. To clearly distinguish different solvent species, atomic colors or representations in the simulation snapshots may vary and are used only to differentiate atoms from different solvent molecules. In hexane/methanol mixtures, methanol enriched at the GO walls while hexane remained excluded from the channel (Fig. 4e and Supplementary Fig. 34), confirming polarity-driven spatial differentiation. In methanol/water mixtures, however, both polar solvents adsorbed along the GO surfaces, producing overlapping distributions and limited spatial differentiation (Fig. 4f and Supplementary Figs. 35, 36). Specifically, polar solvents formed structured interfacial layers along oxygen-rich GO regions, which can act as preferential transport distinct from bulk-like transport. As the channels become tighter and/or less polar, this interfacial segregation weakens and solvent distributions converge, especially for polar/polar mixtures, diminishing

https://doi.org/10.1038/s41467-026-73466-6

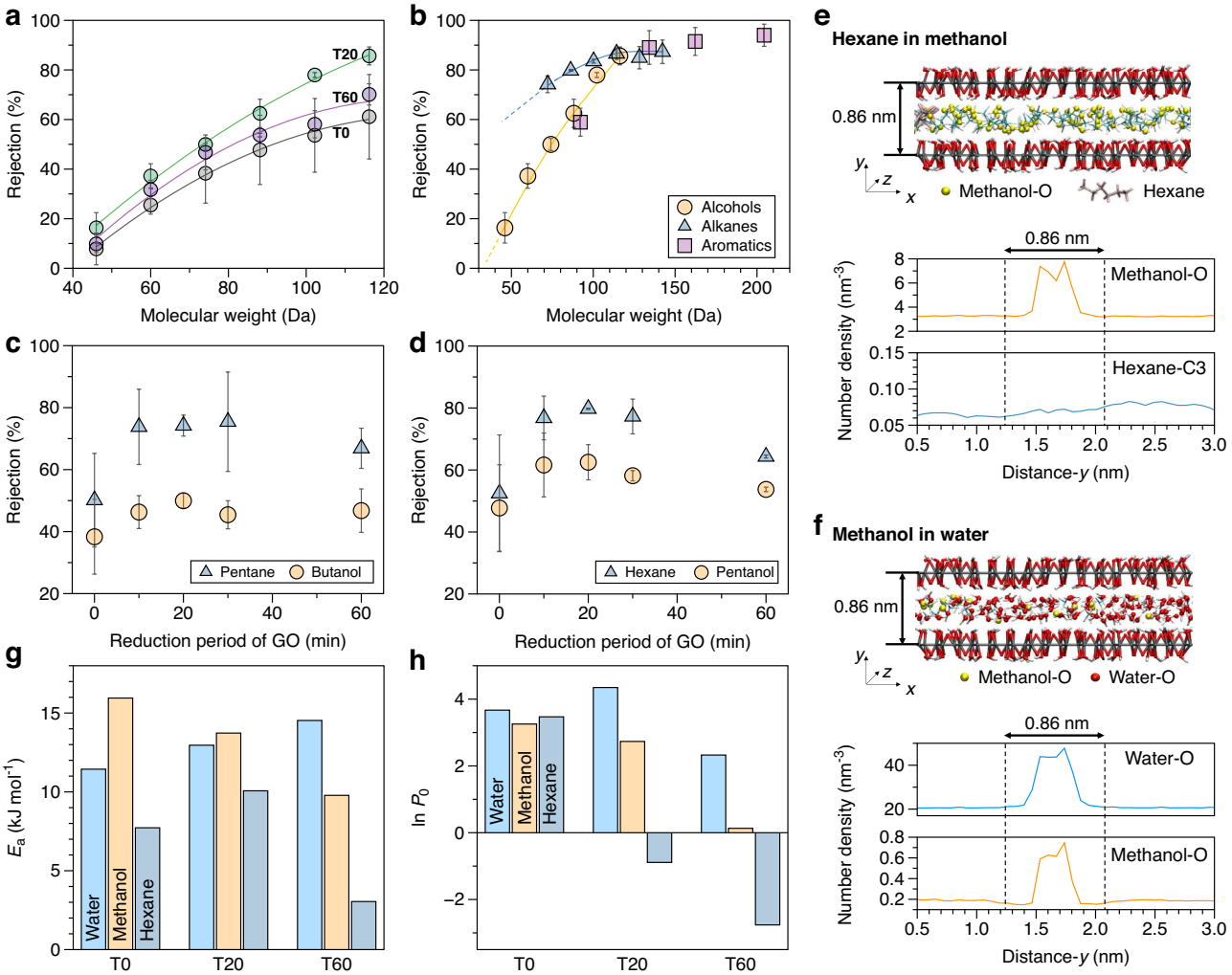

Fig. 4 | Solvent rejection and temperature-derived transport parameters of GO nanochannel membranes. a Rejection of alcohols from alcohol/methanol binary mixtures by GO membranes (T0, T20, and T60 are shown for clarity). **b** Rejection of representative solvent classes from their binary mixtures with methanol by the T20 membrane. Lines in (**a**, **b**) serve as visual guides. **c**, **d** Comparison of rejection between (**c**) pentane and butanol and (**d**) hexane and pentanol in their respective binary mixtures with methanol. Error bars represent the mean ± standard deviation ($n = 2$–4 independent replicates per condition). **e**, **f** Simulation snapshots and number density profiles showing solvent distributions in GO nanochannels for (**e**) hexane/methanol and (**f**) methanol/water mixtures. **g**, **h** Arrhenius-derived parameters for transport in T0, T20, and T60: (**g**) apparent activation energy (E_a) and (**h**) pre-exponential term ($\ln P_0$) extracted from permeance measured at different temperatures. Note: All permeation and separation tests were performed at 30 bar.

selectivity. These results emphasize that maintaining accessible, functionalized interfaces within the channel is essential for selective transport of polar solvents.

To probe transport barriers, we measured the permeance of water, methanol, and hexane over a range of temperatures and fitted the data with an Arrhenius relationship. From the slope and intercept, we extracted an apparent activation energy (E_a) and a pre-exponential term ($\ln P_0$) for each solvent–membrane pair (Fig. 4g, h and Supplementary Fig. 37). We examined three representative membranes of T0, T20, and T60 that span the systematic variations induced by chemical reduction, with T0 exhibiting large channels and high polarity, T20 providing intermediate channel size and moderate polarity, and T60 representing small channels with low polarity. The fitted E_a values were higher for polar solvents (water and methanol), consistent with stronger solvent–GO interactions (e.g., hydrogen bonding and dipolar interactions) and additional reorganization under confinement. Meanwhile, polar solvents also showed higher $\ln P_0$, suggesting a more favorable apparent entropic contribution associated with a large number of accessible transport microstates enabled by their interfacial association and smaller molecular size. T0 showed minimal $\ln P_0$ differentiation, consistent with weak entropic discrimination in large, deformable channels, whereas T20 and T60 displayed more pronounced $\ln P_0$ variation as confinement increased.

Despite these entropy-related trends, both T0 and T60 exhibited only moderate selectivity compared with T20 in filtration experiments, though for different underlying reasons. This underscores that entropy alone cannot explain performance. Instead, separation reflects the combined influence of solvent–channel affinity, which shifts the apparent enthalpic–entropic balance, and nanoconfinement, which limits available transport pathways and molecular configurations. In highly confined channels, a reduced local dielectric environment can amplify the mismatch with bulk solvents and increase barriers for polar molecules[51]. Nevertheless, this effect is counterbalanced by their preferential association with oxygen-rich GO regions, which enables access to interfacial pathways and facilitates permeation. Together with their relatively small size and high configurational freedom, polar solvents permeate more effectively than nonpolar molecules. These findings indicate that affinity-biased interfacial organization, rather than size exclusion alone, governs solvent separation in GO membranes. High selectivity requires not only

https://doi.org/10.1038/s41467-026-73466-6

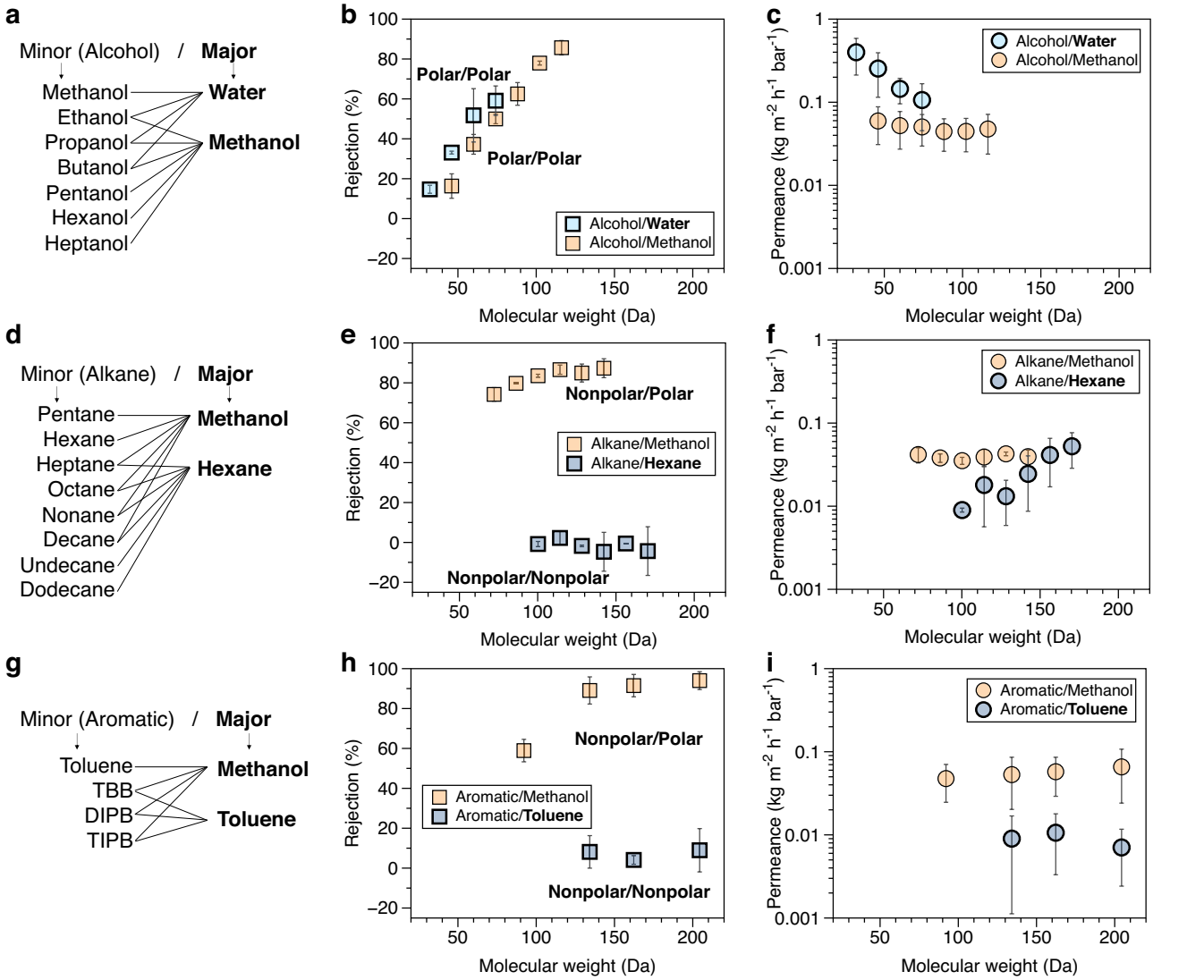

Fig. 5 | Binary solvent-mixture separation by the T20 membrane. **a**, **d**, **g** Combinations of minor- and major-component solvents tested. **b**, **e**, **h** Rejection of the minor-component solvent. **c**, **f**, **i** Mixture permeance. Error bars represent the mean ± standard deviation ($n = 2–4$ independent replicates per condition). Note: All separation tests were performed at 30 bar. Mixture permeance is reported on a mass basis (kg m^{-2} h^{-1} bar^{-1}).

appropriate channel dimensions but also preserved polarity and accessible interfacial pathways, as exemplified by the T20 membrane.

Solvent separation from other mixtures in nanochannels

To broaden the scope beyond methanol-based mixtures, we tested the T20 membrane with binary mixtures consisting of 5 wt% minor-component solvent in 95 wt% major-component solvent, covering polar/polar, nonpolar/polar, and nonpolar/nonpolar combinations. For polar/polar systems (Fig. 5a), alcohol rejection in both water-rich and methanol-rich feeds increased with the molecular weight of the minor alcohol (Fig. 5b). The corresponding mixture permeance decreased with increasing alcohol size in water-rich mixtures, whereas in methanol-rich mixtures it remained similar across the series or showed only a weak downward trend within experimental scatter (Fig. 5c).

To interpret trends across different major-solvent systems (e.g., water-rich versus methanol-rich feeds), it should be noted that a fixed mass fraction does not necessarily translate into the same thermodynamic effective concentration of the minor component. Because the chemical-potential difference in solvent reverse osmosis is concentration-dependent, the net driving force under a fixed applied pressure can differ between solvent systems even at the same mass-fraction feed. In practice, the effective concentration is better described by the activity of the minor component, which depends on both composition and solvent environment. As a practical approximation for cross-system comparisons, matching the mole fraction helps align composition on a consistent basis and reduces discrepancies introduced by differences in the molecular weight of the major solvent. Consistently, composition-variation measurements show that increasing the minor-component level measurably alter both permeance and rejection (Supplementary Fig. 38), underscoring the need for caution in cross-system comparisons. To minimize composition-driven ambiguity, we therefore performed representative mole-fraction-matched controls by adjusting the alcohol content in methanol-rich feeds to match the alcohol mole fraction used in the corresponding water-rich feeds (Supplementary Fig. 39). Under these matched conditions, the water-rich mixtures still exhibited higher alcohol rejection and permeance than the methanol-rich mixtures, consistent with the stronger polarity contrast in the water-rich environment.

For nonpolar/polar mixtures, including alkanes/methanol and aromatics/methanol, nonpolar solvent rejection rose with its size,

https://doi.org/10.1038/s41467-026-73466-6

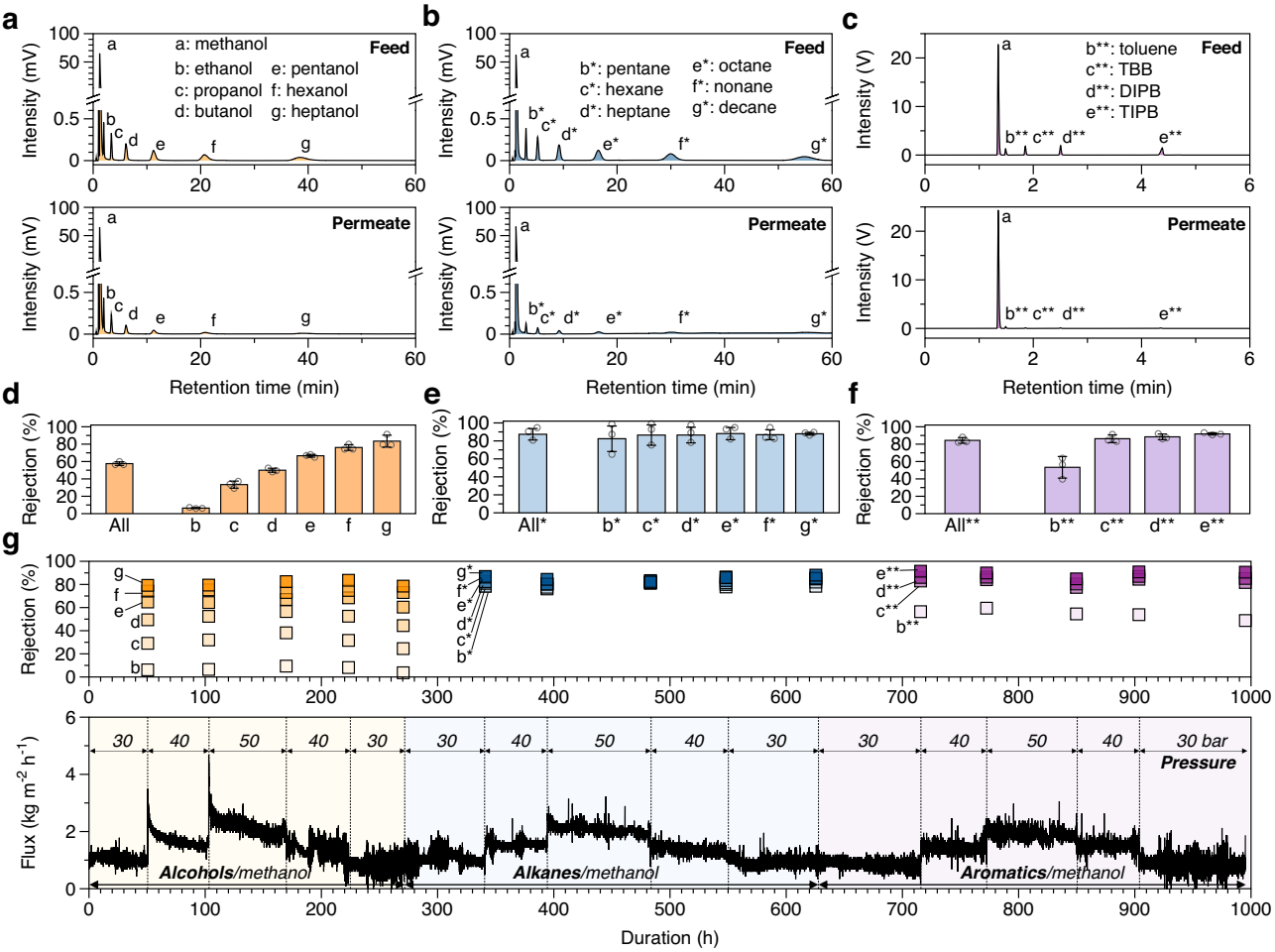

Fig. 6 | Multicomponent solvent-mixture separation by the T20 membrane. **a**–**c** Gas chromatography spectra of feed and permeate samples for methanol-based mixtures containing multiple (**a**) alcohols, (**b**) alkanes, and (**c**) aromatics. In the spectra, the methanol peak is labeled "a"; minor-component peaks are labeled "b–g" (alcohols), "b*–g*" (alkanes), and "b**–e**" (aromatics). **d**–**f** Rejection of the total minor-component fraction and individual components for the (**d**) alcohol, (**e**) alkane, and (**f**) aromatic mixtures. Error bars represent the mean ± standard deviation ($n = 3$ independent replicates). **g** Time-dependent flux and rejection during continuous separation of multicomponent mixtures under cyclic pressure conditions.

reaching ~80% for alkanes up to 100 Da and ~95% for aromatics up to ~200 Da (Fig. 5d–i and Supplementary Figs. 28–31). By contrast, nonpolar/nonpolar systems of alkane/hexane and aromatic/toluene showed negligible rejection regardless of molecular size of the minor component. This absence of selectivity highlights the limits of GO nanochannels in discriminating between chemically similar, weakly interacting solvents. For clarity and comparison, the key numerical metrics for these binary-mixture separations are summarized in Supplementary Table 3. In the alkane/hexane mixtures, permeance tended to increase with larger alkanes, likely due to relatively large alkanes intercalate into the interlayers and perturb the interlayer spacing in this weakly interacting, nonpolar environment. Mechanistically, nonpolar solvents with relatively weak intermolecular forces such as van der Waals interactions exhibited similar transport behavior in GO channels, preventing differentiation by channel-wall chemistry in addition to the absence of size-selectivity effects. While GO nanochannels failed to separate nonpolar mixtures, it reveals that more rigid channels are necessary for such separations.

We next extended separation tests to multicomponent solvent mixtures (Fig. 6a–c) using the T20 membrane. Alcohols/methanol (minor component: from ethanol to heptanol, each 0.5 mol%), alkanes/methanol (minor component: from pentane to decane, each 0.5 mol%), and aromatics/methanol (minor component: toluene, TBB, DIPB, and TIPB, each 0.5 mol%) were filtered at 30 bar. In all cases, larger and less polar solvents showed higher rejection, and overall rejection levels (~ 60% for alcohols, ~87% for alkanes, ~85% for aromatics, Fig. 6d–f) were consistent with binary mixture behavior. This consistency indicates that size–polarity mechanisms governing binary systems also extend to more complex mixtures.

To assess operational robustness, long-term tests were conducted under cyclically varied pressures (30–50 bar) for each type of multicomponent feed mixtures over a total duration of ~1000 h (Fig. 6g). Flux showed transient increases after step changes in pressure during initial alcohols/methanol separation process, likely from temporary pressure change-induced structural relaxation[52], but then stabilized at each pressure (Supplementary Fig. 40) with rejection maintained. No degradation was observed across repeated cycles, confirming that the T20 membrane sustains selective performance under realistic, high-pressure solvent conditions.

Taken together, these results establish that GO nanochannel membranes separate solvent mixtures through a dual dependence on molecular size and polarity based on permeation studies across 18 pure solvents, 30 binary mixtures, and 3 multicomponent systems. Strong polarity contrasts drive effective rejection, while weakly interacting nonpolar mixtures are not effectively separated. The T20 membrane demonstrates that carefully balanced channel size and surface polarity enable both high selectivity and structural stability, extending from binary to multicomponent systems and sustaining

performance under long-term, varied pressurized operation. More broadly, the results point to a polarity-matching design rule for polar solvent reverse osmosis in 2D nanochannels, linking channel chemistry and confinement to the polarity landscape of the solvent system.

Discussion

Solvent reverse osmosis places solvent molecules in a confined environment where interfacial interactions and geometric restriction jointly shape transport. Here, the combined experiments and simulations show that solvent distributions and mobilities within laminated GO nanochannels shift systematically with oxidation degree and channel tightness, as evidenced by near-wall enrichment/exclusion and distinct interfacial-layer mobility, revealing interfacial association as a key contributor to selectivity in polarity-sensitive mixtures.

A key implication is that molecular size alone does not predict transport across chemically diverse liquids. In polarity-rich or polarity-contrast systems, interfacial affinity can amplify subtle molecular differences and enable discrimination among sub-100 Da solvents, whereas chemically similar nonpolar mixtures show limited differentiation under comparable confinement. Channel chemistry and the local dielectric environment therefore become design variables as consequential as channel size. Consistent with this view, recent studies on cross-linked polymeric membranes with engineered functionalities likewise show that tuning membrane–solvent affinity can improve hydrocarbon retention from alcohol-rich feeds[38,39], underscoring interfacial affinity as a general principle for liquid-phase solvent separations.

Solvent reverse osmosis operates entirely in the liquid phase, which is attractive for continuous solvent recovery and purification, especially when high-boiling solvents are involved and alternative routes such as extraction or adsorption often introduce additional solvents, regeneration cycles, or thermal steps. Even for weakly differentiable polar–polar mixtures (e.g., alcohol/alcohol), where single-stage fractionation is intrinsically limited, solvent reverse osmosis can serve as a pressure-driven enrichment step for dehydration or preconcentration[53,54], and thus integrate naturally into hybrid separation trains.

The solvent-dependent separation behavior observed here further emphasizes that solvent reverse osmosis is a materials-matching problem. In nonpolar-rich environments (aromatic- or hydrocarbon-dominated mixtures), GO nanochannels can be perturbed by intercalation of weakly interacting, larger hydrocarbons. This response reflects a solvent–material mismatch rather than a fundamental limitation of laminated 2D architectures. Nonpolar-rich systems instead demand tighter interlayer cohesion, reduced susceptibility to solvent-induced dilation, and solvent-specific stabilization strategies. Such requirements can be met through alternative 2D materials and post-assembly approaches, including cross-linking, interlayer locking, and chemical functionalization[55]. Notably, stabilization concepts established for aqueous environments may not translate directly to nonpolar media, highlighting the need for solvent-specific design.

Beyond polarity, confinement can also magnify weaker but specific interaction features. For example, π–π affinity between aromatic solvents and conjugated or graphitic channel walls can favor interfacial association and modulate transport, enabling discrimination of aromatics from alkanes that is largely independent of size differences and overall nonpolarity[6,56]. Together, these considerations suggest that effective solvent reverse osmosis membranes should be designed by aligning dominant solvent–membrane affinities with stabilized confinement, whether the governing affinity is polarity-driven, aromaticity-driven, or otherwise interaction-specific.

Overall, laminated 2D nanochannels provide a tunable architecture where localized functionalization modulates interfacial affinity without altering the laminated framework, enabling mechanistic insight and rational membrane design beyond size exclusion. While GO serves here as a chemically tractable model system, the resulting principles provide a transferable basis for co-engineering affinity and confinement in more complex membrane materials and pore architectures.

Methods

Chemical modification of GO

A 10 mL aqueous suspension containing 0.15 mg GO, 1.5 mg glucose, and 40 μL of ammonia solution (28–30 wt%), was vigorously mixed. The mixture was then heated at 95 °C for varying durations of 10, 20, 30, and 60 min to achieve different reaction extents before being cooled to 25 °C for further use.

Membrane fabrication

Porous PK membranes were prepared using the nonsolvent-induced phase separation method. In short, PK powder was dissolved in an aqueous solution with 35 wt% resorcinol to reach a concentration of 14 wt%. The polymer dope solution was stirred at 80 °C until the PK completely dissolved. It was kept in an oven at 50 °C and left to settle for at least 24 h to remove air bubbles before further use. To fabricate the membranes, the PK dope solution was cast onto either a bare glass plate or nonwoven fabric attached to a glass plate, forming free-standing PK membranes or PK/fabric membranes. A casting knife set to a gap of 400 μm controlled the thickness. After casting, the glass plate was immersed in a coagulation bath containing 35 wt% methanol and 65 wt% water for phase separation, resulting in a solid white PK membrane. Subsequently, the membrane was soaked sequentially in acetone and hexane for 20 min each to eliminate any residual solvent. Finally, the membranes were dried and stored at room temperature (25 °C).

GO membranes were fabricated by a vacuum filtration assembly process. Porous membrane supports of nylon, PK, or PK/fabric served as filters for depositing the pristine or modified GO nanosheets. An aqueous suspension containing 0.15 mg of nanosheets was diluted to 300 mL with ultrapure water and sonicated before vacuum filtration. After the water from the suspension was completely filtered, the support membrane with the deposited nanosheets was dried in a desiccator for at least 24 h before further use.

Membrane filtration tests

Membrane coupons were sealed in a home-made stainless steel cross-flow stirred cell with an effective membrane area of ~7.1 cm^2 for pure solvent permeation and solvent mixture filtration experiments. Flow rate of 60 mL min^{-1}, stirring speed of 500 rpm, and pressure of 30 bar were applied for the filtrations unless otherwise specified. Pure solvent, binary solvent mixtures, and multicomponent solvent mixtures were used as feed for different tests. For the binary solvent mixtures, a composition of 95 wt% of major-component solvent and 5 wt% of minor-component solvent was used while for the multicomponent solvent mixtures, each minor-component concentration was fixed at 0.5 mol%.

The mass (M, kg) of permeate from the cross-flow filtration was continuously monitored using an electronic balance (GF-1000, A&D Co., Ltd., Tokyo, Japan). Solvent permeance was measured and reported at steady state. The permeation flux (F, L m^{-2} h^{-1}), volume-based permeance (P_V, L m^{-2} h^{-1} bar^{-1}) for pure solvent permeation, and weight-based permeance for solvent mixture permeation (P_M, kg m^{-2} h^{-1} bar^{-1}) of the membrane were calculated using the following equations:

$$F = \frac{V}{At} \tag{1}$$

$$P_V = \frac{V}{At\triangle p} \tag{2}$$

$$P_M = \frac{M}{At\triangle p} \quad (3)$$

where V (L) is the volume of the collected permeate; A (m^2) is the effective membrane area; t (h) is the filtration duration; and $\triangle p$ is the operation pressure (bar).

Permeance of water, methanol, and hexane was measured under different temperatures to obtain activation energy (E_a) and pre-exponential factor (ln P_0) by fitting the data into linearized Arrhenius plot:

$$\ln P_V = -\frac{E_a}{R} \times \frac{1}{T} + \ln P_0 \quad (4)$$

where R is the universal gas constant (0.08314 L bar K^{-1} mol^{-1}); T is the absolute temperature (K).

To determine the composition of feed and permeate solvent mixtures, one gas chromatography with thermal conductivity detector (GC-2014, Shimadzu Corp., Kyoto, Japan) and another one with flame ionization detector (GC-2030, Shimadzu Corp., Kyoto, Japan) were used depending on the specific types of solvent mixtures. GC calibration was performed using an external standard method. Calibration curves were established using standard solutions of known concentrations and used to determine sample concentrations. Membrane rejection (Rej, %) was calculated based on following equation:

$$\text{Rej} = \left(1 - \frac{C_p}{C_f}\right) \times 100\% \quad (5)$$

Where C_p and C_f are minor-component solvent concentrations in permeate and feed samples, respectively.

During the filtration tests, the feed composition was considered constant due to large volume used and limited filtrated amount. Membrane permeance and rejection data were reported upon a steady state of membrane performance was achieved.

Characterizations

Mechanical strength of porous polymer supports was measured by a precision strength tester (AGS-J, Shimadzu Corp., Kyoto, Japan), with a sample length of approximately 10 mm and a fixed extension rate of 10 mm min^{-1}. The morphologies of the membrane samples were observed using field-emission SEM (JSF-7500F, JEOL Co. Ltd., Tokyo, Japan) at an accelerating voltage of 5 kV. Prior to imaging, the samples were coated with a thin osmium layer to enhance surface conductivity and reduce charging effects. XPS (JPS-9010 MC, JEOL Co. Ltd., Tokyo, Japan) was performed using an Al Kα radiation source (1486.6 eV) to analyze the membrane surface chemistry. XRD (Ultima IV, Rigaku, Tokyo, Japan) was used to reveal the interlayered channel dimensions of the GO laminates, with a step size of 0.02° and scanning speed of 5° min^{-1}. For the measurement of the wet samples, methanol droplets were gradually added to the surface of the sample until complete surface coverage was achieved. After 5 min of wetting, the excessive methanol drops on the membrane surface was carefully removed using lab tissue paper and then subjected to XRD analysis. The water and diiodomethane contact angles of the different membrane samples were analyzed using a contact angle testing system (DMo-502, Kyowa Interface Science Co., Ltd., Tokyo, Japan).

Simulation methods

Molecular simulations were performed to complement the experimental observations. Three GO models with O/C ratios of 0.2, 0.3, and 0.4 were constructed based on the Lerf–Klinowski model, representing different oxidation degrees with corresponding interlayer spacings of 7.6–8.6 Å. These models were used to calculate polarity descriptors, analyze solvent distributions and dynamics, and evaluate GO–solvent interaction energies. Pure solvents of water, methanol, and hexane, as well as representative binary solvent mixtures of methanol/water (5:95 or 50:50, w/w) and hexane/methanol (5:95, w/w) were simulated. All molecular dynamics simulations were carried out using the Gromacs 2019.6 package with Amber- and GAFF-based force fields, and the results were analyzed to extract solvent density profiles and mean square displacements. Interaction energies were calculated using the GFN2-xTB method through xtb 6.7.1 program. Full simulation protocols, including force field parameterization, system setup, and calculation procedures, are provided in the Supplementary Information.

Data availability

The data supporting the findings of this study are available within the paper and its Supplementary Information files. The quantum-mechanically optimized geometries, as well as the initial and final configurations from molecular dynamics simulations, have been deposited in Materials Cloud at https://doi.org/10.24435/materialscloud:56-nn. Source data are provided with this paper.

References

1. Sholl, D. S. & Lively, R. P. Seven chemical separations to change the world. *Nature* **532**, 435–437 (2016).
2. Liu, C., Dong, G., Tsuru, T. & Matsuyama, H. Organic solvent reverse osmosis membranes for organic liquid mixture separation: A review. *J. Membr. Sci.* **620**, 118882 (2021).
3. Kopecek, J. Performance of Porous Cellulose Acetate Membranes for the Reverse Osmosis Separation of Mixtures of Organic Liquids. *Ind. Eng. Chem. Process Des. Dev.* **9**, 5–12 (1970).
4. Fang, Y., Sourirajan, S. & Matsuura, T. Reverse osmosis separation of binary organic mixtures using cellulose acetate butyrate and aromatic polyamide membranes. *J. Appl. Polym. Sci.* **44**, 1959–1969 (1992).
5. Koh, D.-Y., McCool, B. A., Deckman, H. W. & Lively, R. P. Reverse osmosis molecular differentiation of organic liquids using carbon molecular sieve membranes. *Science* **353**, 804–807 (2016).
6. Thompson, K. A. et al. N-Aryl–linked spirocyclic polymers for membrane separations of complex hydrocarbon mixtures. *Science* **369**, 310–315 (2020).
7. Li, S. et al. Hydrophobic polyamide nanofilms provide rapid transport for crude oil separation. *Science* **377**, 1555–1561 (2022).
8. Chisca, S. et al. Polytriazole membranes with ultrathin tunable selective layer for crude oil fractionation. *Science* **376**, 1105–1110 (2022).
9. Guan, K. et al. Thin film composite membrane with improved permeance for reverse osmosis and organic solvent reverse osmosis. *J. Membr. Sci.* **688**, 122104 (2023).
10. Ren, Y. et al. Fluorine-rich poly(arylene amine) membranes for the separation of liquid aliphatic compounds. *Science* **387**, 208–214 (2025).
11. Lee, T. H. et al. Microporous polyimine membranes for efficient separation of liquid hydrocarbon mixtures. *Science* **388**, 839–844 (2025).
12. Lively, R. P. & Sholl, D. S. From water to organics in membrane separations. *Nat. Mater.* **16**, 276–279 (2017).
13. Nunes, S. P. et al. Thinking the future of membranes: Perspectives for advanced and new membrane materials and manufacturing processes. *J. Membr. Sci.* **598**, 117761 (2020).
14. Kim, J., Kim, J. F., Jiang, Z. & Livingston, A. G. Advancing membrane technology in organic liquids towards a sustainable future. *Nat. Sustain.* **8**, 594–605 (2025).
15. Lu, X. & Elimelech, M. Fabrication of desalination membranes by interfacial polymerization: history, current efforts, and future directions. *Chem. Soc. Rev.* **50**, 6290–6307 (2021).

16. Branton, D. et al. The potential and challenges of nanopore sequencing. *Nat. Biotechnol.* **26**, 1146–1153 (2008).
17. El-Sayed, M. A. Some Interesting Properties of Metals Confined in Time and Nanometer Space of Different Shapes. *Acc. Chem. Res.* **34**, 257–264 (2001).
18. Maier, J. Nanoionics: ion transport and electrochemical storage in confined systems. *Nat. Mater.* **4**, 805–815 (2005).
19. Shen, J. et al. Engineering grain boundaries in monolayer molybdenum disulfide for efficient water-ion separation. *Science* **387**, 776–782 (2025).
20. He, Z., Zhou, J., Lu, X. & Corry, B. Bioinspired Graphene Nanopores with Voltage-Tunable Ion Selectivity for Na+ and K+. *ACS Nano* **7**, 10148–10157 (2013).
21. Shen, J., Liu, G., Han, Y. & Jin, W. Artificial channels for confined mass transport at the sub-nanometre scale. *Nat. Rev. Mater.* **6**, 294–312 (2021).
22. Chen, L. et al. Ion sieving in graphene oxide membranes via cationic control of interlayer spacing. *Nature* **550**, 380–383 (2017).
23. Liu, G., Jin, W. & Xu, N. Two-Dimensional-Material Membranes: A New Family of High-Performance Separation Membranes. *Angew. Chem. Int. Ed.* **55**, 13384–13397 (2016).
24. Wang, Z. et al. Graphene oxide nanofiltration membranes for desalination under realistic conditions. *Nat. Sustain.* **4**, 402–408 (2021).
25. Xia, Y. et al. Polymeric membranes with aligned zeolite nanosheets for sustainable energy storage. *Nat. Sustain.* **5**, 1080–1091 (2022).
26. Dai, L. et al. Sodium-Ion Traps in a Two-Dimensional Confined Channel for Effective Water and Ion Selective Transport. *Nano Lett.* **24**, 13686–13694 (2024).
27. Jiang, W. et al. Axial alignment of covalent organic framework membranes for giant osmotic energy harvesting. *Nat. Sustain.* **8**, 446–455 (2025).
28. Dong, X. et al. Heteropolyacid Ligands in Two-Dimensional Channels Enable Lithium Separation from Monovalent Cations. *ACS Nano* **19**, 4233–4241 (2025).
29. Wang, X. et al. Comediation of voltage gating and ion charge in MXene membrane for controllable and selective monovalent cation separation. *Sci. Adv.* **10**, eado3998 (2024).
30. Wang, H. et al. Covalent organic framework membranes for efficient separation of monovalent cations. *Nat. Commun.* **13**, 7123 (2022).
31. Ortiz-Young, D., Chiu, H.-C., Kim, S., Voïtchovsky, K. & Riedo, E. The interplay between apparent viscosity and wettability in nanoconfined water. *Nat. Commun.* **4**, 2482 (2013).
32. Chen, X. et al. Nanoscale Fluid Transport: Size and Rate Effects. *Nano Lett.* **8**, 2988–2992 (2008).
33. Nazari, M., Davoodabadi, A., Huang, D., Luo, T. & Ghasemi, H. Transport Phenomena in Nano/Molecular Confinements. *ACS Nano* **14**, 16348–16391 (2020).
34. Thomas, J. A. & McGaughey, A. J. H. Reassessing Fast Water Transport Through Carbon Nanotubes. *Nano Lett.* **8**, 2788–2793 (2008).
35. Nie, L. et al. Realizing small-flake graphene oxide membranes for ultrafast size-dependent organic solvent nanofiltration. *Sci. Adv.* **6**, eaaz9184 (2020).
36. Shinde, D. B. et al. Crystalline 2D Covalent Organic Framework Membranes for High-Flux Organic Solvent Nanofiltration. *J. Am. Chem. Soc.* **140**, 14342–14349 (2018).
37. Van Buggenhout, S. et al. Open and FAIR data for nanofiltration in organic media: A unified approach. *J. Membr. Sci.* **713**, 123356 (2025).
38. Zhang, A. et al. Polar Pore Surface of Polyamide Membranes Enabling Efficient Solvent Mixture Separation. *Adv. Funct. Mater.* **35**, 2422376 (2025).
39. Li, J. et al. Spirocyclic poly(vinylene ether ketone) membranes with enhanced microporosity for energy-efficient alcohol-hydrocarbon azeotrope separation. *Nat. Commun.* **16**, 10000 (2025).
40. Guan, K. et al. Interfacial polymerization of thin film selective membrane layers: Effect of polyketone substrates. *J. Membr. Sci.* **640**, 119801 (2021).
41. Pocivavsek, L. et al. Stress and Fold Localization in Thin Elastic Membranes. *Science* **320**, 912–916 (2008).
42. Dreyer, D. R., Park, S., Bielawski, C. W. & Ruoff, R. S. The chemistry of graphene oxide. *Chem. Soc. Rev.* **39**, 228–240 (2010).
43. Zheng, S., Tu, Q., Urban, J. J., Li, S. & Mi, B. Swelling of Graphene Oxide Membranes in Aqueous Solution: Characterization of Interlayer Spacing and Insight into Water Transport Mechanisms. *ACS Nano* **11**, 6440–6450 (2017).
44. Zheng, S., Tu, Q., Wang, M., Urban, J. J. & Mi, B. Correlating Interlayer Spacing and Separation Capability of Graphene Oxide Membranes in Organic Solvents. *ACS Nano* **14**, 6013–6023 (2020).
45. Marchetti, P., Jimenez Solomon, M. F., Szekely, G. & Livingston, A. G. Molecular Separation with Organic Solvent Nanofiltration: A Critical Review. *Chem. Rev.* **114**, 10735–10806 (2014).
46. Karan, S., Jiang, Z. & Livingston, A. G. Sub–10 nm polyamide nanofilms with ultrafast solvent transport for molecular separation. *Science* **348**, 1347 (2015).
47. Shen, L. et al. Highly porous nanofiber-supported monolayer graphene membranes for ultrafast organic solvent nanofiltration. *Sci. Adv.* **7**, eabg6263 (2021).
48. Yang, Q. et al. Ultrathin graphene-based membrane with precise molecular sieving and ultrafast solvent permeation. *Nat. Mater.* **16**, 1198–1202 (2017).
49. Lu, T. & Chen, F. Multiwfn: A multifunctional wavefunction analyzer. *J. Comput. Chem.* **33**, 580–592 (2012).
50. Lu, T. Sobtop, Version [1.0(dev3)]. http://sobereva.com/soft/Sobtop/ (accessed on Aug. 9th, 2022) (2022).
51. Fumagalli, L. et al. Anomalously low dielectric constant of confined water. *Science* **360**, 1339–1342 (2018).
52. Guan, K. et al. Deformation constraints of graphene oxide nanochannels under reverse osmosis. *Nat. Commun.* **14**, 1016 (2023).
53. Hu, M. et al. Isopropanol concentration by osmotically assisted reverse osmosis. *J. Membr. Sci.* **697**, 122581 (2024).
54. Hu, M. et al. Concentration of high boiling point organic solvents by osmotically assisted reverse osmosis. *Water Res* **282**, 123929 (2025).
55. Chen, X. & Wang, H. Graphene oxide patchwork membranes. *Nat. Nanotechnol.* **16**, 226–227 (2021).
56. Liu, C. et al. Regulating the Layered Stacking of a Covalent Triazine Framework Membrane for Aromatic/Aliphatic Separation. *Angew. Chem. Int. Ed.* **63**, e202320137 (2024).

Acknowledgements

This work is dedicated to Professor Hideto Matsuyama on the occasion of his retirement, in honor of his visionary leadership as the founding director of the Research Center for Membrane and Film Technology at Kobe University, Japan. The authors are deeply grateful for his lifelong dedication to membrane science and for the inspiring mentorship he continues to provide. This study was conducted within the framework of the International Membrane Hub.

Author contributions

K.G., W.J. and H.M. conceived and designed the research. K.G. carried out membrane fabrication, characterization, and performance testing. Y.G. (Yanan Guo) and Y.G. (Yuanyuan Guo) performed computational simulations and analyses. L.D., A.Z., Z.L. and E.D. assisted with characterizations and performance evaluation. K.G., W.J., G.L., H.M., K.N. and T.Y. interpreted the data. K.G., K.N., Y.G. (Yanan Guo), G.L., W.J. and H.M. wrote and revised the manuscript.

Funding
This study was supported by the Kao Foundation for Arts and Sciences (K.G.), the Kobe University Strategic International Collaborative Research Grant Type B: Fostering Joint Research (H.M.), and the National Natural Science Foundation of China (Nos. 22038006 for W.J. and 22308149 for Y.G.). The authors also acknowledge the High Performance Computing Center of Nanjing Tech University for providing computational resources.

Competing interests
The authors declare no competing interests.

Additional information
Supplementary information The online version contains supplementary material available at https://doi.org/10.1038/s41467-026-73466-6.

Correspondence and requests for materials should be addressed to Yanan Guo, Wanqin Jin or Hideto Matsuyama.

Peer review information *Nature Communications* thanks Tongxi Lin, and the other, anonymous, reviewer(s) for their contribution to the peer review of this work. A peer review file is available.

Reprints and permissions information is available at http://www.nature.com/reprints

Publisher's note Springer Nature remains neutral with regard to jurisdictional claims in published maps and institutional affiliations.

Open Access This article is licensed under a Creative Commons Attribution-NonCommercial-NoDerivatives 4.0 International License, which permits any non-commercial use, sharing, distribution and reproduction in any medium or format, as long as you give appropriate credit to the original author(s) and the source, provide a link to the Creative Commons licence, and indicate if you modified the licensed material. You do not have permission under this licence to share adapted material derived from this article or parts of it. The images or other third party material in this article are included in the article's Creative Commons licence, unless indicated otherwise in a credit line to the material. If material is not included in the article's Creative Commons licence and your intended use is not permitted by statutory regulation or exceeds the permitted use, you will need to obtain permission directly from the copyright holder. To view a copy of this licence, visit http://creativecommons.org/licenses/by-nc-nd/4.0/.

© The Author(s) 2026